SPECIAL ISSUE ARTICLE

FFEMS Fatigue & Fracture of Engineering Materials & Structures   WILEY

High-cycle and very-high-cycle fatigue behavior at two stress ratios of Ti-6Al-4V manufactured via laser powder bed fusion with different surface states

Rui Fu[1] | **Liang Zheng**[1] | **Zheng Zhong**[1] | **Youshi Hong**[2] ⓘ

[1]School of Science, Harbin Institute of Technology (Shenzhen), Shenzhen, China

[2]LNM, Institute of Mechanics, Chinese Academy of Sciences, Beijing, China

Correspondence
Zheng Zhong, School of Science, Harbin Institute of Technology (Shenzhen), Shenzhen 518055, China.
Email: zhongzheng@hit.edu.cn

Youshi Hong, LNM, Institute of Mechanics, Chinese Academy of Sciences, Beijing 100190, China.
Email: hongys@imech.ac.cn

Abstract

The high-cycle fatigue (HCF) and very-high-cycle fatigue (VHCF) behavior of Ti-6Al-4V manufactured by laser powder bed fusion (L-PBF) was investigated to reveal the effects of surface roughness and stress ratio on fatigue performance. Fatigue tests were performed by an ultrasonic vibration machine with a frequency of 20 kHz. The fatigue strength of surface-polished specimens is generally higher than that of as-built specimens in HCF and VHCF regimes. Fatigue cracks initiated from the subsurface of as-built and surface-polished L-PBF Ti-6Al-4V. The values of size and depth for the defects that acted as fatigue crack origins present large scattering for L-PBF Ti-6Al-4V due to the interaction between surface roughness and subsurface defects. For surface-polished L-PBF Ti-6Al-4V, fatigue cracks have almost the same resistance to propagation at both stress ratios of $R = -1$ and 0.7.

KEYWORDS

laser powder bed fusion, stress ratio, surface roughness, Ti-6Al-4V, very-high-cycle fatigue

Highlights

- Fatigue strength of surface-polished specimens higher than as-built L-PBF Ti-6Al-4V
- Fatigue crack initiation from lack-of-fusion defects in subsurface defect-enriched layer
- Defect & surface roughness with greater effect on crack initiation than stress ratio
- Crack propagation much easier in as-built than surface-polished L-PBF Ti-6Al-4V

1 | INTRODUCTION

The technique of additive manufacturing (AM) was first introduced in the late 1980s, driven by the need for rapid prototyping of models.[1] In the past decade, the rapid

---

development of additive manufacturing has led to the emergence of the promising technologies such as rapid proto-typing, direct digital manufacturing, etc. AM, also called 3D printing, is a technology that three-dimensional components made of metals, ceramics or other materials can be manufactured layer by layer based on a 3-D CAD solution.[2,3] It can quickly and accurately produce parts of any complex shape with simpler processing procedure, shorter processing time and fewer amount of materials in comparison with conventional manufacturing methods. Therefore, with the development of AM technology, more and more components in biomedicine, aerospace, power industry and other industrial fields are manufactured by AM, in which titanium alloys (e.g., Ti-6Al-4V) are one of the typical kinds due to its low density, high strength, good biocompatibility and excellent corrosion resistance.[4–6] The commonly-used AM techniques for Ti-6Al-4V parts include laser powder bed fusion (L-PBF),[7–9] electron beam powder bed fusion (EB-PBF),[10–12] directed energy deposition (DED)[13–15] and cold spray additive manufacturing (CSAM),[16] among which L-PBF has advantages of small dimensions and high productivity.[17] In engineering practice, L-PBF Ti-6Al-4V parts are often subjected to a long period of cyclic load during their service lives, for example, heart valve implants are subjected to about 1×10^8 cycles and aircraft propel blades are subjected to about 1×10^9 cycles in their entire service lives.[18,19] Hence, it is imperative to investigate high-cycle-fatigue (HCF) and very-high-cycle-fatigue (VHCF) behavior of L-PBF Ti-6Al-4V to understand related mechanisms and thus, to improve their fatigue properties.

A number of studies have shown that the fatigue behavior of L-PBF Ti-6Al-4V was mainly affected by the surface roughness, internal defects such as porosity and lack-of-fusion (LOF) defects, microstructure inhomogeneity and residual stresses.[20–22] In particular, surface and internal defects are often recognized as the fatigue crack origins for L-PBF Ti-6Al-4V.[23,24] Especially, the contour scanning of L-PBF process that is used to define the manufactured shape, always induces a considerable amount of defects (pores) in the subsurface layer. On one hand, surface post-treatment processes on complex geometry parts are not always feasible so that surface roughness still plays an important role in the alteration of fatigue behavior of L-PBF Ti-6Al-4V.[25–27] It has been shown that surface roughness can be regarded as micro-notches and hence some representative parameters of surface roughness are employed to describe the surface morphology.[23,28,29] Furthermore, several models considering the effect of surface roughness have been used to estimate the fatigue strength/life of AM parts in HCF regime.[30–34] On the other hand, some studies have shown that heat-treatment processes such as hot isostatic pressing (HIP) may be applied to diminish the internal defects so as to enhance the fatigue performance of L-PBF Ti-6Al-4V, but it is almost impossible to reduce the amount of surface defects.[35–37] Hence, many studies have been carried out to investigate the effect of surface roughness on the fatigue properties of L-PBF alloys.[38–40] However, the effect of surface roughness on the fatigue behavior of L-PBF Ti-6Al-4V up to VHCF regime under as-built surface condition is rarely reported and the related crack initiation mechanism is still unclear.

For VHCF failure, it is well known that the competitive relationship of crack initiation between surface and internal modes is an important scientific issue.[41–43] For conventionally manufactured metallic materials, internal crack initiation is dominant,[44–46] but surface crack initiation may occur for some materials such as titanium alloy.[47,48] Nevertheless, typical characteristics, for example, surface and internal defects, of L-PBF Ti-6Al-4V are generated during manufacturing process, which makes the fatigue crack initiation behavior and mechanism much more complicated than conventionally manufactured titanium alloys. In particular, for L-PBF Ti-6Al-4V with as-built surface condition, whether the crack will initiate from surface or internal/subsurface is directly affected by the interaction between surface roughness and internal/subsurface defects.[30,35,49] In brief, the effects of surface roughness and subsurface defects on the fatigue behavior of L-PBF Ti-6Al-4V have attracted much attention in the related field. However, the mechanism regarding the influence of surface roughness and/or subsurface defects on the fatigue behavior up to VHCF regime for L-PBF Ti-6Al-4V with as-built surface condition is still unclear.

It has been widely recognized that stress ratio (R) or mean stress has a significant effect on the fatigue behavior of AMed titanium alloys.[50–52] For example, Benedetti et al.[53] studied the effects of applied stress ratios ($R = -3$, -1 and 0.1) on the compression-compression low-and high-cycle fatigue behaviors of heat-treated L-PBF Ti-6Al-4V, and stated that the HCF behavior is mainly affected by the extent of mean stress and defects. Du et al.[54] studied the effects of stress ratios ($R = -1$ and 0.5) on the VHCF behavior of heat-treated L-PBF Ti-6Al-4V and found that fatigue cracks initiated from LOF defects for both stress ratios. In the case of porous L-PBF Ti-6Al-4V parts, Krijger et al.[55] studied the effects of stress ratios ($R = 0.1, 0.3, 0.5, 0.7$ and 0.8) on fatigue performance in HCF regime, and revealed that the *S-N* curves shift upwards as the stress ratio increases. Most recently, our experimental investigations[56] showed that the stress ratios ($R = -1, -0.5, 0.1$ and 0.5) have a significant effect on the fatigue performance and crack

initiation characteristics up to VHCF regime of heat-treated L-PBF Ti-6Al-4V. However, the correlation between stress ratio and fatigue behavior of L-PBF Ti-6Al-4V in VHCF regime under as-built surface condition is unclear and needs in-depth investigation.

In this paper, the fatigue behavior in HCF and VHCF regimes of L-PBF Ti-6Al-4V is comprehensively investigated and the effects of surface roughness, subsurface defects and stress ratio on fatigue performance are addressed. First, tensile and fatigue test specimens of Ti-6Al-4V were manufactured by L-PBF. Then a quasi-static tensile test was performed to obtain the tensile strength and yield strength of L-PBF Ti-6Al-4V. Ultrasonic fatigue tests with a frequency of 20 kHz were carried out at different stress ratios ($R = -1$ and 0.7) for the specimens with different surface roughness (as-built and surface-polished). All the fracture surfaces of failed specimens were examined by scanning electron microscopy (SEM), and the equivalent size and depth of defects that acted as fatigue crack origins were measured via Image-Pro Plus 6.0 software. Finally, the mechanisms of fatigue crack initiation and early propagation induced by defects were discussed. The results of this investigation are meaningful for extending the service lives of titanium alloy parts and may provide useful reference for improving fatigue properties of L-PBF Ti-6Al-4V. Especially, this paper pays specific attention to the defects in the subsurface layer induced by the contour scanning of L-PBF process, which will be useful for the case that the subsurface defects of AMed parts are hardly or impossible to be eliminated.

2 | MATERIALS AND EXPERIMENTAL METHODS

As one type of L-PBF processes, an SLM125 AM machine was used to manufacture Ti-6Al-4V specimens, and the processing parameters are listed in Table 1. The input energy density (E) of the L-PBF process is given by[57]

$$E = \frac{P}{V \times d \times h} \quad (1)$$

where P is laser power, V is scan speed, d is layer thickness, and h is hatch spacing. By using the values provided in Table 1, E was calculated as 69.44 W·s/mm³. Figure 1A shows the schematic of the L-PBF process[58] and the sweeping action in the process is by a rake. Figure 1B shows the SEM image and the particle size distribution of the Ti-6Al-4V powder produced by gas atomization in argon atmosphere. All specimens were fabricated in an argon-filled chamber and the laser traveling direction was rotated by 30° for the subsequent layer to minimize the anisotropy of L-PBF Ti-6Al-4V specimens. It is seen from Figure 1B that most of Ti-6Al-4V powder particles are spherical and the diameters of the particles follow a Gaussian distribution with the mean value of 32 μm (d50) and the standard deviation of 64 μm².

All L-PBF Ti-6Al-4V specimens were directly printed according to the shape and dimensions of the tensile (Figure 1C) and fatigue (Figure 1D) specimens. Among them, the design of ultrasonic fatigue specimens satisfies

TABLE 1 Processing parameters of L-PBF Ti-6Al-4V.

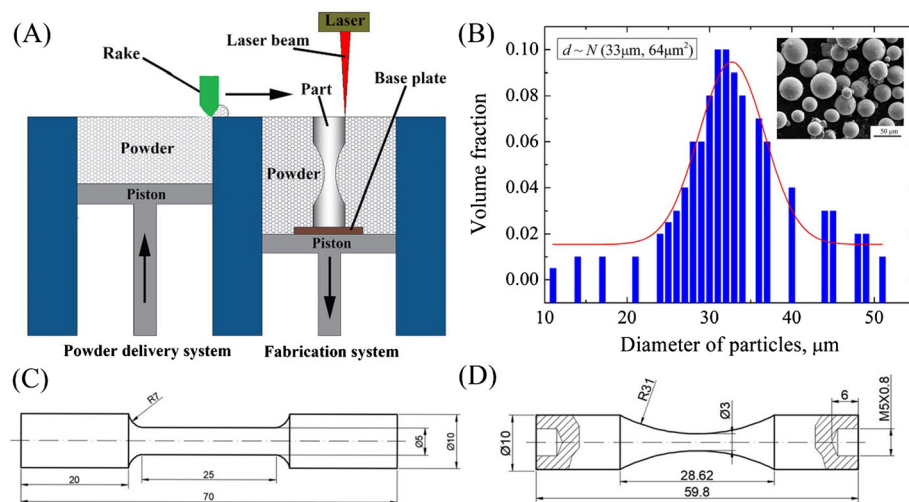| P (W)	V (mm/s)	Print direction	Laser path deflection	h (mm)	d (mm)
325	1300	z-axis	30°	0.12	0.03

FIGURE 1 (A) Schematic of laser powder bed fusion (L-PBF) process,[58] (B) scanning electron microscopy (SEM) image and particle size distribution of Ti-6Al-4V powder, shape and dimensions (mm) of tensile test specimen (C) and ultrasonic fatigue test specimen (D). [Colour figure can be viewed at wileyonlinelibrary.com]

the resonant condition for 20 kHz testing frequency. The chemical composition of present L-PBF Ti-6Al-4V specimens was analyzed by X-ray photoelectron spectroscopy (XPS, ESCALAB 250Xi, Thermo Fisher, UK) and listed in Table 2. The hardness test of L-PBF Ti-6Al-4V was performed on a Vickers hardness tester (Duranmin-40, Struers, Denmark) under a 500 g load for 10 s dwell time with an indenter of diamond tip. The value of hardness was determined by taking the average value after excluding the highest and lowest values among 10 measurements of the Vickers hardness. Tensile tests with the strain rate of 10^{-4} s^{-1} were performed to obtain tensile strength and yield strength of L-PBF Ti-6Al-4V. For microstructural observation, two samples with the size of 3 mm × 3 mm × 1 mm were cut from a tensile specimen along the horizontal cross-section and longitudinal cross-section, respectively. Such samples were ground with sandpapers with 180–5000 grit, polished with a mixture of 70% SiO_2 colloid and 30% H_2O_2, etched with Kroll reagent for about 15 s (100 mL water, 1 to 3 mL hydrofluoric acid, 2 to 6 mL nitric acid mixture) and finally examined via an optical microscope (OM, VHX-900F, Japan). An electron backscatter diffraction (EBSD, TSL Hikari Super, TSL, USA) was utilized to clarify the crystal structure and preferred orientation of L-PBF Ti-6Al-4V. The EBSD system combined with a field-emission scanning electron microscope (SEM, FEI Apreo S, USA) and AZtecHKL v3.1 software was used to obtain the EBSD data.

3 | RESULTS

3.1 | Mechanical properties and microstructure of L-PBF Ti-6Al-4V

The Vickers hardness test showed that the hardness of L-PBF Ti-6Al-4V specimens is 367 HV. Tensile test results showed that the tensile strength and yield strength of L-PBF Ti-6Al-4V are 1202 MPa and 1068 MPa, respectively, which are close to the results in Du et al.[54] For comparison, the tensile strength and yield strength of conventionally rolled[47] Ti-6Al-4V are 945 and 812 MPa, respectively, which are smaller than those of L-PBF Ti-6Al-4V. This indicates that microstructure refinement with acicular α' feature (as shown in Figure 2) can increase the tensile strength and yield strength of L-PBF Ti-6Al-4V. Figure 2A,B illustrates the OM images showing the microstructure of L-PBF and rolled[59] Ti-6Al-4V, respectively. It is seen that the microstructure of L-PBF Ti-6Al-4V is mainly composed of acicular α' feature (hexagonal closed-packed lattice structure), whereas the microstructure of rolled[59] Ti-6Al-4V is dual-phase structure. The difference in the microstructure of L-PBF and rolled Ti-6Al-4V results from their manufacturing processes. The L-PBF manufacturing is a very fast solidifying process, which makes the produced parts with a very fine lamellar microstructure consisting almost acicular α' martensites within columnar prior β grains, whereas the rolled Ti-6Al-4V has a low cooling rate during the manufacturing process, which allows the transition from β to α phase thus to produce an equiaxed bimodal microstructure. Figure 3A,B presents the EBSD images showing the microstructure and preferred orientation of L-PBF Ti-6Al-4V at horizontal and longitudinal cross-sections, respectively. It is clearly observed that acicular α' texture at the horizontal/longitudinal cross-sections shows a strong uniformity in orientation along their horizontal (A2)/longitudinal (A1) axes. In the $\{0001\}_\alpha$ pole figures shown in Figure 3C,D, the maximum intensity is 31.85 at horizontal cross-sections and 22.30 at longitudinal cross-sections, which implies that a strong crystallographic texture of L-PBF Ti-6Al-4V is in the $\{0001\}_\alpha$ plane. Therefore, the preferred orientations of $\{0001\}_\alpha$ may lead to strong anisotropy in the mechanical properties of L-PBF Ti-6Al-4V and the effect

TABLE 2 Chemical composition of L-PBF Ti-6Al-4V.

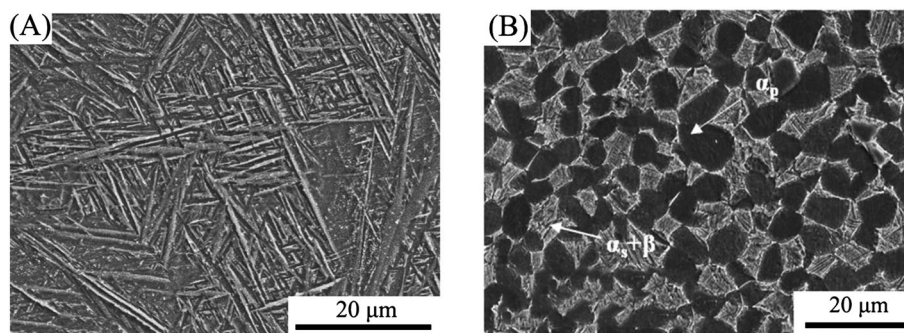| Element	Al	V	O	C	Fe	N	Ti
Weight (wt.%)	6.02	3.97	0.10	0.01	0.03	0.01	balance

FIGURE 2 Optical microscope (OM) images showing microstructures of (A) L-PBF and (B) rolled[59] Ti-6Al-4V alloys.
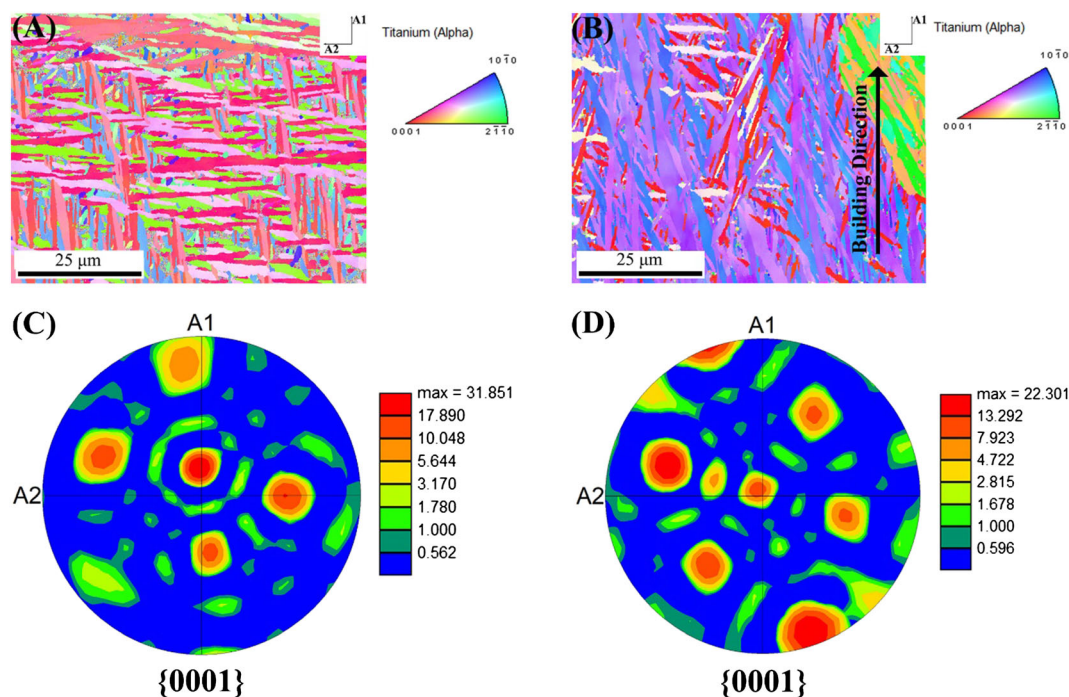
FIGURE 3 Electron backscatter diffraction (EBSD) images of (A) horizontal cross-section and (B) longitudinal cross-section for L-PBF Ti-6Al-4V, the corresponding {0001}$_\alpha$ pole figures of (C) horizontal cross-section and (D) longitudinal cross-section. [Colour figure can be viewed at wileyonlinelibrary.com]

of anisotropy on the fatigue properties was reported in the literature.[38,49] The average thickness of single α' lamellae of L-PBF Ti-6Al-4V was measured as 1.5 μm, which is similar to the result in Gong et al.,[60] but much smaller than that of rolled Ti-6Al-4V (5.89 μm, measured in Liu et al.[59]).

3.2 | Surface states of L-PBF Ti-6Al-4V

During the printing process, each specimen was manufactured by means of a hatching plus contour scan procedure. During contour scanning, a laser at a power a bit lower than 325 W was used to define the outer shape, and then during the inner hatching, a laser at 325 W was applied to print the inner structure of each layer. This printing method often results in a large difference in the subsurface and internal microstructure of the manufactured parts. Figure 4A,B presents the OM images showing the horizontal cross-section microstructure of as-built and surface-polished L-PBF Ti-6Al-4V specimens, respectively. It is seen that there is a defect-enriched layer near the surface for both as-built and surface-polished specimens. Note that similar results were reported in Macallister and Becker.[39] The values of thickness of the defect-enriched layer (T) were measured via image-Pro Plus 6.0 software to get $T = 150$ μm and $T = 120$ μm for

the as-built and surface-polished specimens, respectively. In order to quantitatively characterize the defect size distribution within the defect-enriched layer, the sizes of the defects observed on the fracture surfaces of failed specimens were measured by the use of Image-Pro Plus 6.0 software. Figure 4C,D shows the defect size distribution within the defect-enriched layer for as-built specimens and surface-polished specimens, respectively. The horizontal axis is the equivalent defect size, $\sqrt{area}$, proposed by Murakami,[61] and the vertical axis is the frequency. It is seen that the defect size distribution for as-built specimens is close to that for surface-polished specimens, which follows the Cauchy distribution. The defect sizes are in the range of 5–95 μm with most of them distribute from 5 to 65 μm. It is worth noting that the defect-enriched layer is quite thick, which is 150 μm for the as-built specimens and 120 μm for surface-polished specimens. The crack initiation sites in HCF and VHCF regimes are almost located in this defect-enriched layer (This will be addressed later in this paper). In addition, the defects in the inner region away from the defect-enriched layer are very limited with very small size; that is, the inner region is almost a "clean" region compared to the defect-enriched layer.

For the purpose of further estimating the characteristics of the defects of L-PBF Ti-6Al-4V, the following equation was employed to express porosity φ:
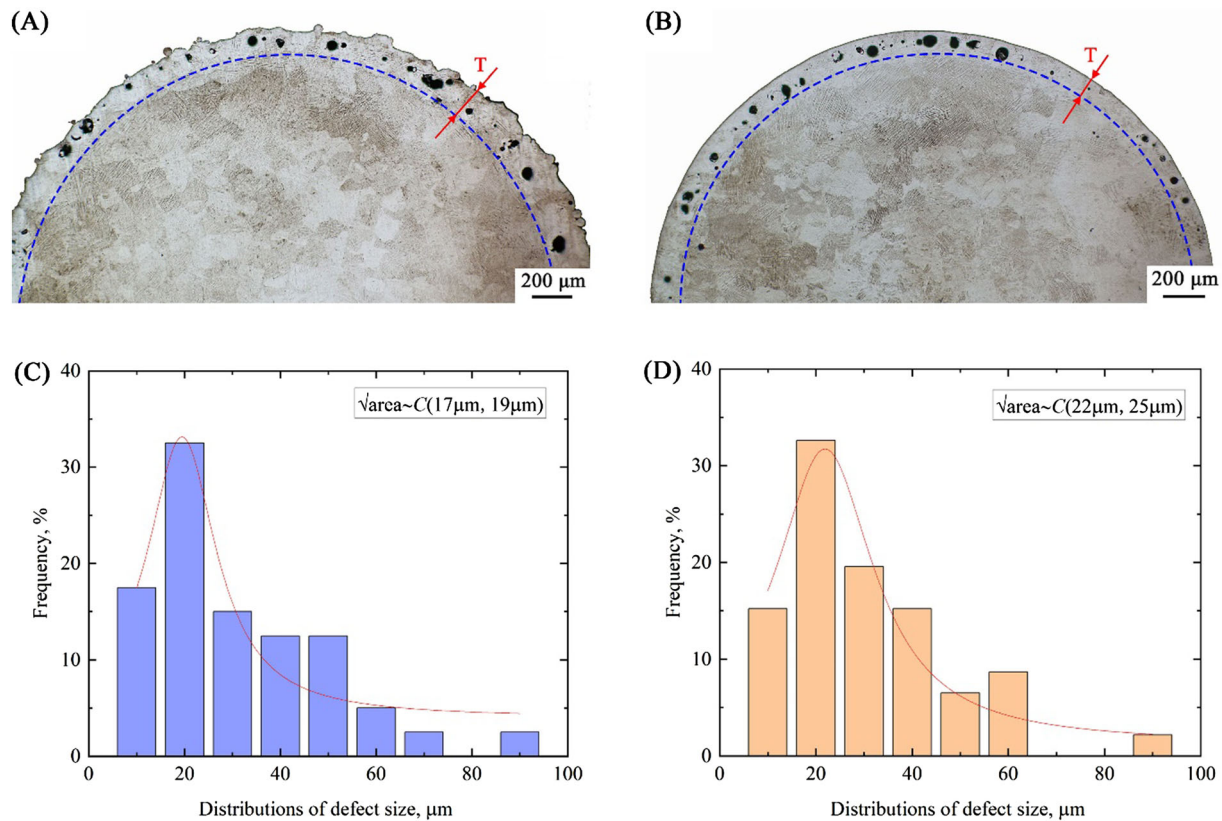
FIGURE 4 Optical microscopy images showing defect distribution of laser powder bed fusion (L-PBF) specimens: (A) as-built and (B) surface-polished, defect size distribution within the defect-enriched layer for (C) as-built specimens and (D) surface-polished specimens. [Colour figure can be viewed at wileyonlinelibrary.com]

$$\varphi = \left(1 - \frac{\rho}{\rho_0}\right) \times 100\% \qquad (2)$$

where ρ is the density of L-PBF Ti-6Al-4V, and ρ_0 is the nominal density of defect-free counterpart obtained via rolled Ti-6Al-4V samples. The densities of the samples were measured by using Archimedes method[60] to give $\rho = 4.374$ g/cm^3 for as-built L-PBF Ti-6Al-4V samples, $\rho = 4.382$ g/cm^3 for surface-polished L-PBF Ti-6Al-4V samples and $\rho_0 = 4.506$ g/cm^3 for rolled Ti-6Al-4V samples. Therefore, the porosities were calculated to be 2.93% for as-built specimens and 2.75% for surface-polished specimens, which implies that the porosity of as-built L-PBF Ti-6Al-4V is slightly larger than that of surface-polished L-PBF Ti-6Al-4V due to different surface states.

In order to clearly characterize the surface state of the L-PBF Ti-6Al-4V, surface roughness of the specimens was measured by a scanning white light interferometer (SWLI) of ZYGO Nexview. Two parameters are used as the indicators of the surface profile of the L-PBF Ti-6Al-4V specimens, namely, the average roughness (R_a) and the maximum height of the profile (R_t), in which R_t is defined as the vertical distance between the highest peak

and lowest valley along the sampling length,[62] and R_a is calculated via Equation (3):

$$R_a = \frac{1}{l} \int_0^l |y(x)| \, dx \qquad (3)$$

where l is the sampling length and $y(x)$ is the profile height from the mean line.

Figure 5 shows the results of surface profile and associated parameters for L-PBF Ti-6Al-4V specimens and the load direction is parallel to the building direction. Figure 5A illustrates the 3-D SWLI image of the as-built specimen and Figure 5B presents the 1-D surface profile given by the line ($x = 400$ μm) in Figure 5A. Similar results are given in Figure 5C,D. Results in Figure 5B,D indicate that the surface roughness values for as-built specimens are much larger (R_a: 10.3 μm and R_t: 63.2 μm) than that of surface-polished specimens (R_a: 1.25 μm and R_t: 6.89 μm). Large surface roughness may induce relatively large stress concentration, which will increase the possibility of crack initiation. Similar arguments were reported in previous works.[11,32]
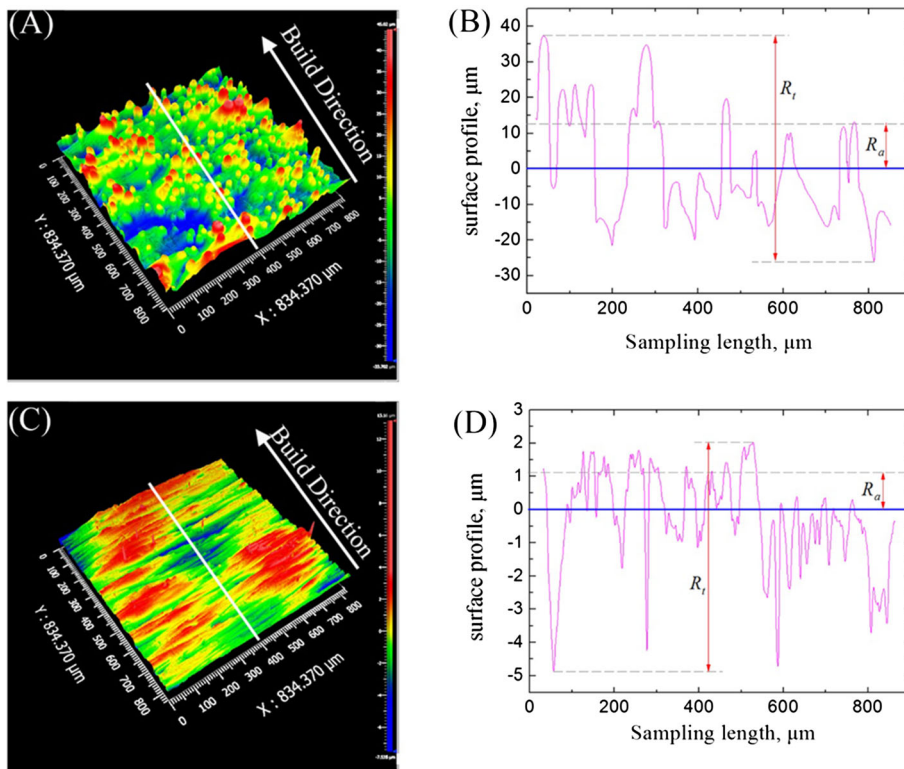
FIGURE 5 Surface profile and associated representing parameters for laser powder bed fusion (L-PBF) Ti-6Al-4V specimens, (A) 3-D scanning white light interferometer (SWLI) image of an as-built specimen, (B) relation between sampling length and 1-D surface profile of (A), (C) 3-D SWLI image of a surface polished specimen, and (D) relation between sampling length and 1-D surface profile of (C). [Colour figure can be viewed at wileyonlinelibrary.com]

3.3 | S-N data

Figure 6 illustrates the *S-N* data presented by double-logarithmic plot of ultrasonic fatigue tests for L-PBF Ti-6Al-4V with different surface roughness (as-built and surface-polished) and stress ratios ($R = -1$ and 0.7). In the plot, the data points with arrows represent run-out specimens at 10^9 loading cycles. Figure 6 indicates that the applied stress amplitude of as-built L-PBF Ti-6Al-4V specimens decreases rapidly from 420 to 50 MPa in HCF regime but presents a horizontal asymptote trend in VHCF regime. For surface-polished L-PBF Ti-6Al-4V specimens at $R = -1$, the applied stress amplitude decreases quickly from 420 to about 130 MPa in HCF regime and has a plateau trend. Then it declines gradually from 130 to 80 MPa in VHCF regime. It is clearly that the *S-N* curve presents a step-wise or duplex shape, and the applied stress amplitude exhibits a sharp decrease in the VHCF regime. For surface-polished L-PBF Ti-6Al-4V specimens at $R = 0.7$, the applied stress amplitude exhibits a steady decrease from 110 to 50 MPa from HCF regime to VHCF regime. In addition, there is a fatigue limit about 50 MPa for as-built L-PBF Ti-6Al-4V specimens, but no evident fatigue limit shown for surface-polished L-PBF Ti-6Al-4V specimens.

It is seen from Figure 6 that the applied stress amplitude of as-built specimens presents a relatively larger scattering in HCF regime than that in VHCF regime, which can be explained as follows. On one hand, the
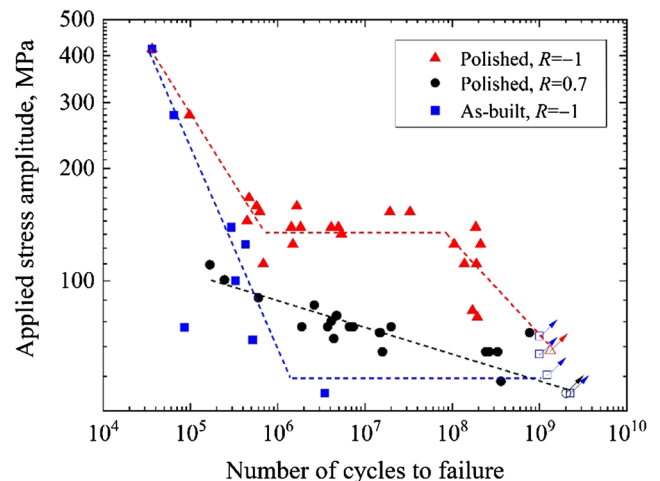

FIGURE 6 *S-N* data of laser powder bed fusion (L-PBF) Ti-6Al-4V specimens, data points with arrows representing run-out specimens at 10^9 cycles. [Colour figure can be viewed at wileyonlinelibrary.com]

applied stress amplitude in HCF regime is relatively large, which may result in the stress concentration at the surface defects similar to that at subsurface defects. On the other hand, the applied stress amplitude in VHCF regime is lower than that in HCF regime, which may result in the stress concentration at surface defects lower than that at subsurface defects. Hence, the fatigue behavior and mechanism of crack initiation are directly

—WILEY—

affected by the interaction between surface roughness and subsurface defects in HCF regime, but mainly affected by subsurface defects in VHCF regime. In addition, the applied stress amplitude of surface-polished specimens at $R = -1$ and 0.7 presents a similar scattering in HCF regime and in VHCF regime, due to the fact that crack initiation is mainly affected by subsurface defects. Figure 6 also reveals that under the same stress ratio ($R = -1$), the fatigue strength of surface-polished specimens is higher than that of as-built specimens, implying that the fatigue strength can be improved by surface polishing. Studies in the literature[35,38,63] indicated that post-treatments such as surface polish, annealing and HIP processing play important roles in the improvement of fatigue strength for L-PBF Ti-6Al-4V. In particular, the fatigue strength of surface-polished L-PBF Ti-6Al-4V with no HIP processing was higher than that of as-built L-PBF Ti-6Al-4V with HIP process,[35] inferring that fatigue strength is markedly affected by surface roughness. In addition, the fatigue limit of rolled[64] Ti-6Al-4V is about 450 MPa, which is the same as that of heat-treated[64] L-PBF Ti-6Al-4V, but much larger than that of as-built specimens in this study. This indicates that surface roughness has a significant effect on the degradation of fatigue strength of as-built L-PBF Ti-6Al-4V than that of heat-treated L-PBF Ti-6Al-4V. In short, surface roughness and stress ratio have significant effects on the fatigue properties of L-PBF Ti-6Al-4V.

3.4 | Fractographic morphologies

Figure 7 illustrates the fractographic morphologies of as-built specimens failed in HCF regime at $R = -1$, in which fatigue cracks initiated from subsurface or the defect-enriched layer with one or multiple crack origins. It is evident that the behavior and mechanism of fatigue crack initiation are affected by the interaction between surface roughness and subsurface defects, similar to the results in previous works.[33,35] Figure 8 presents the fractographic morphologies of surface-polished specimens at $R = -1$, revealing that fatigue cracks initiated from the subsurface with a single crack origin in HCF and VHCF regimes and such origins were generated by LOF defects on the subsurface. Comparison of the results in Figures 7 and 8 reveals that the larger the surface roughness is, the easier the fatigue cracks tend to initiate at multiple origins, inferring that surface roughness has a significant effect on the crack initiation of L-PBF Ti-6Al-4V. For surface-polished specimens at $R = 0.7$, it is seen from Figure 9 that fatigue cracks mainly initiated from subsurface LOF defects, which is similar to that at $R = -1$, but with one exceptional specimen, for which the fatigue crack initiated from multiple LOF defects on the subsurface (Figure 9F). It indicates that stress ratio has an insignificant effect on the type of crack initiation for surface-polished specimens in HCF and VHCF regimes.

In addition, the rough area (RA), which is regarded as the characteristic region of crack initiation,[41] does not appear in either the as-built or surface-polished specimens. The formation mechanism of RA can be explained by the numerous cyclic pressing (NCP) model proposed by Hong et al.,[44] which clarifies that the formation mechanism of RA for the titanium alloy is in relation to stress ratio, fatigue life and defect size. In particular, enough contact pressure and sufficient loading cycles are the necessary requirements for the formation of RA. For as-built and surface-polished specimens in HCF regime, RA
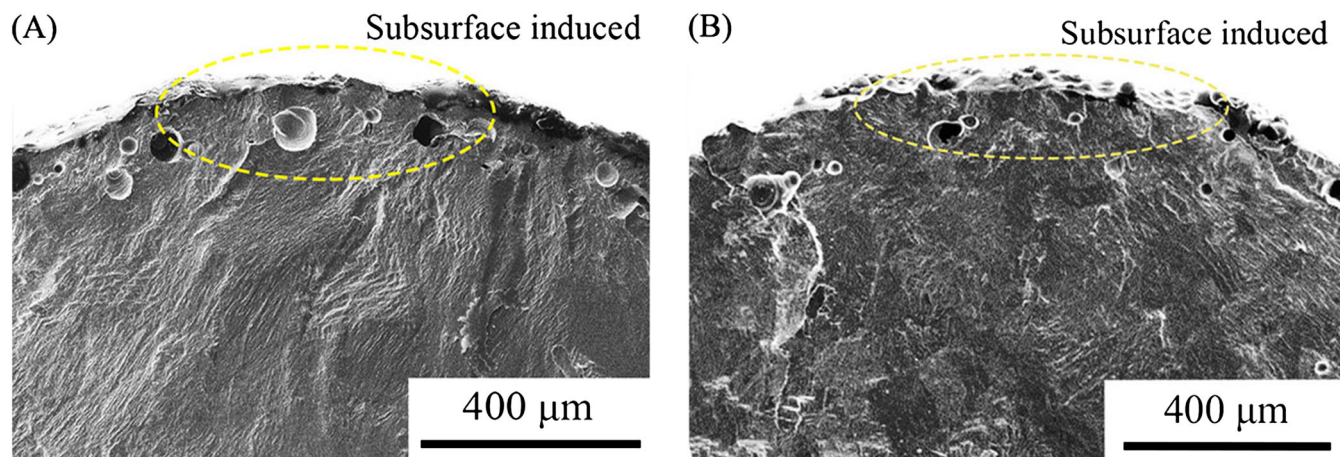

FIGURE 7 Scanning electron microscopy (SEM) images showing fractographic morphologies of as-built specimens failed in HCF regime at $R = -1$, (A) subsurface crack initiation ($\sigma_{max} = 139.1$ MPa and $N_f = 2.9 \times 10^5$), (B) subsurface crack initiation ($\sigma_{max} = 125.2$ MPa and $N_f = 4.3 \times 10^5$). [Colour figure can be viewed at wileyonlinelibrary.com]
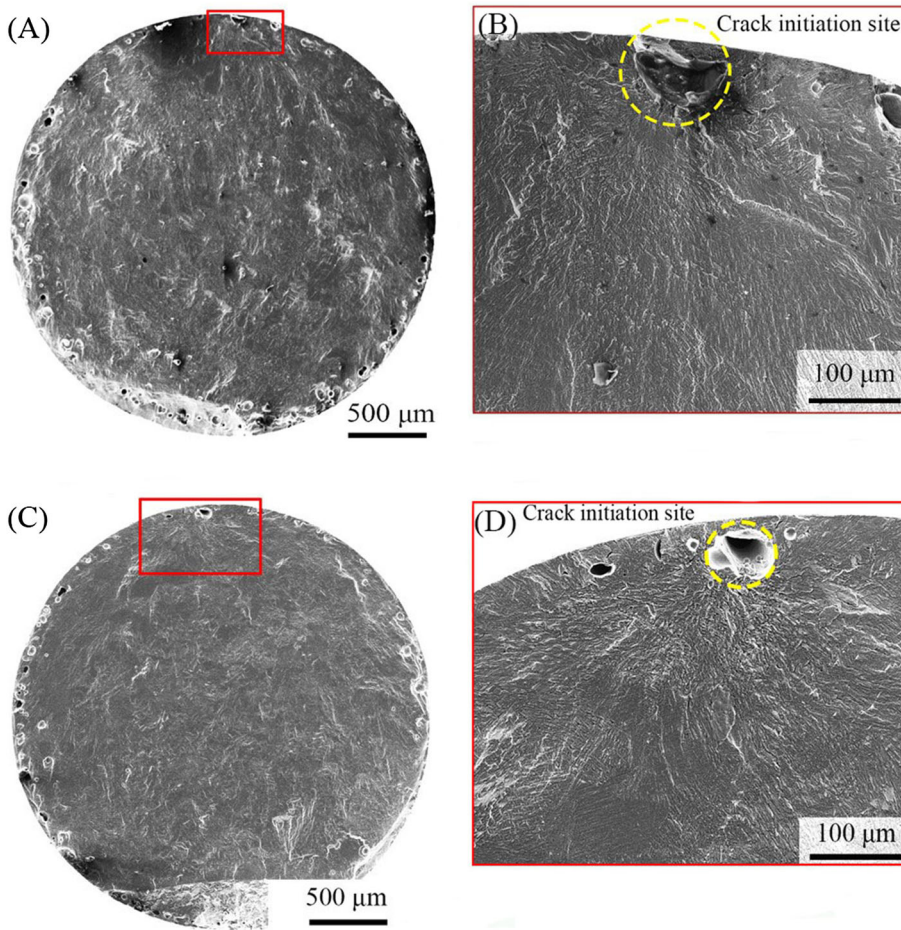
FIGURE 8 Scanning electron microscopy (SEM) images showing fractographic morphologies of surface-polished Ti-6Al-4V at $R = -1$, (A) entire fracture surface ($\sigma_{max} = 139.1$ MPa and $N_f = 1.8 \times 10^6$), (B) magnified image of crack initiation region in (A), (C) entire fracture surface ($\sigma_{max} = 153.0$ MPa and $N_f = 3.3 \times 10^7$), (D) magnified image of crack initiation region in (C). [Colour figure can be viewed at wileyonlinelibrary.com]

cannot be formed due to a lack of sufficient loading cycles. For surface-polished specimens at $R = 0.7$, no RA appearance is in VHCF regime, which is ascribed to a lack of enough contact pressure. It is interesting that no RA morphology was observed in VHCF regime for surface-polished specimens at $R = -1$, which may be attributed to the interaction between surface roughness and subsurface defects. These results are the first revelation of fractographic characteristics in crack initiation region of L-PBF Ti-6Al-4V failed in HCF and VHCF regimes.

4 | DISCUSSION

4.1 | Equivalent size of surface and subsurface defects

Present experimental results have shown that subsurface crack initiation is dominant for L-PBF Ti-6Al-4V, which can be attributed to the interaction between surface roughness and subsurface defects. The equivalent defect size, $\sqrt{area}$, proposed by Murakami,[61] was employed to quantify the relationship between surface/subsurface

defects and the fatigue performance. For as-built specimens, the equivalent defect size $\sqrt{area}$ is presented by the combination of equivalent surface roughness ($\sqrt{area_R}$) and equivalent subsurface defects ($\sqrt{area_D}$). For surface-polished specimens, it is only presented by equivalent subsurface defects ($\sqrt{area_D}$). It is seen from Figure 10 that the surface roughness $\sqrt{area_R}$ can be obtained by using an empirical equation dependent on a and $2b$ of surface roughness, which is expressed as follows[65]:

$$\frac{\sqrt{area_R}}{2b} = 2.97\left(\frac{a}{2b}\right) - 3.51\left(\frac{a}{2b}\right)^2 - 9.74\left(\frac{a}{2b}\right)^3, \text{ for } \frac{a}{2b} \leq 0.195 \quad (4)$$

$$\frac{\sqrt{area_R}}{2b} \approx 0.38, \quad \text{for } \frac{a}{2b} \geq 0.195 \quad (5)$$

where a represents the maximum height, which is R_t in the plot, and $2b$ denotes the average value of peak-to-peak distance. The average values of a and $2b$ can be measured by using SWLI method and they are 63.2 and 52.7 μm for as-built specimens, respectively. Therefore,

FIGURE 9 Scanning electron microscopy (SEM) images showing fractographic morphologies of surface-polished Ti-6Al-4V at $R = 0.7$, (A) entire fracture surface ($\sigma_{max} = 140$ MPa and $N_f = 6.6 \times 10^6$), (B) magnified image of crack initiation region in (A), (C) entire fracture surface ($\sigma_{max} = 135$ MPa and $N_f = 7.7 \times 10^8$), (D) magnified image of crack initiation region in (C), (E) entire fracture surface ($\sigma_{max} = 120$ MPa and $N_f = 1.6 \times 10^7$), and (F) magnified image of crack initiation region in (E). [Colour figure can be viewed at wileyonlinelibrary.com]
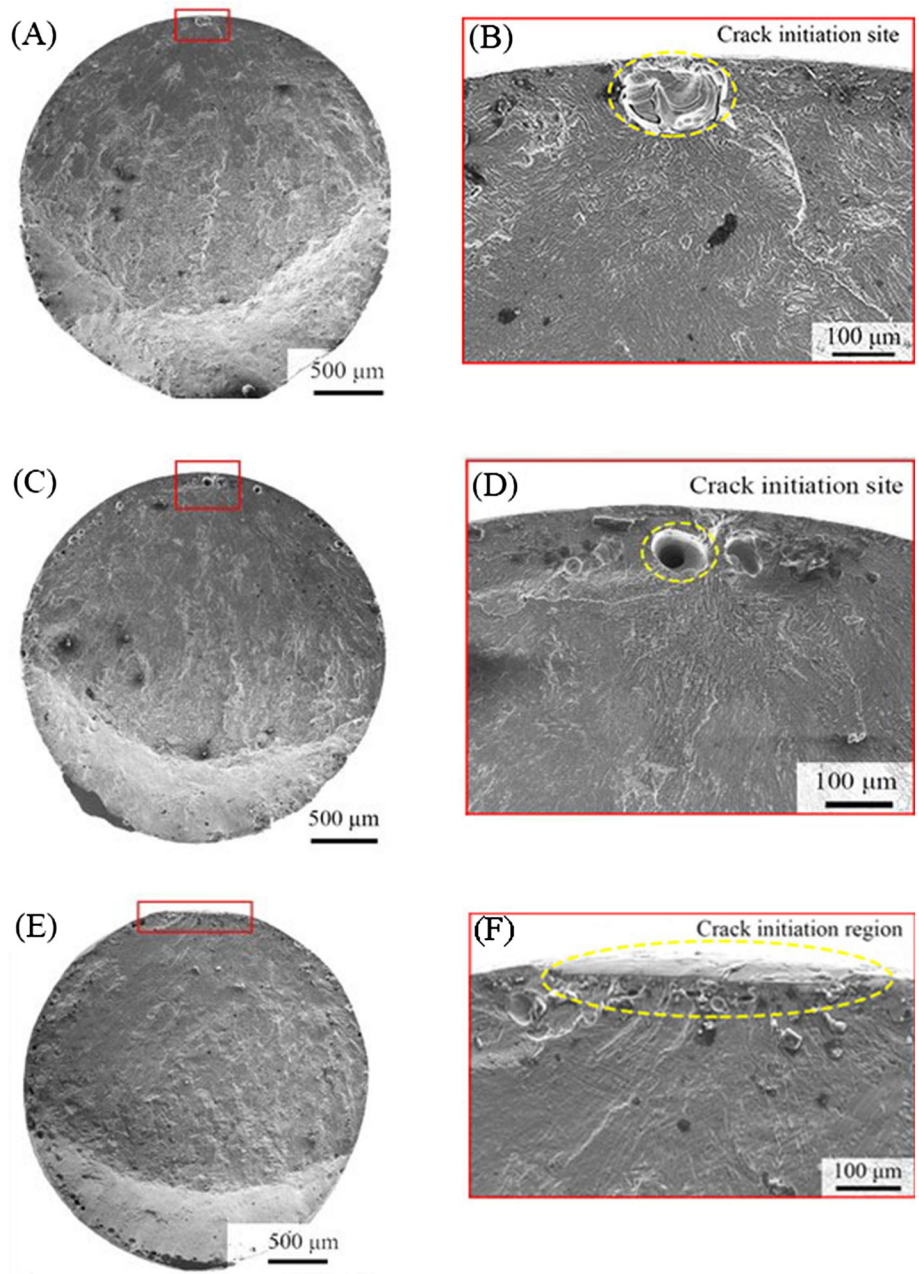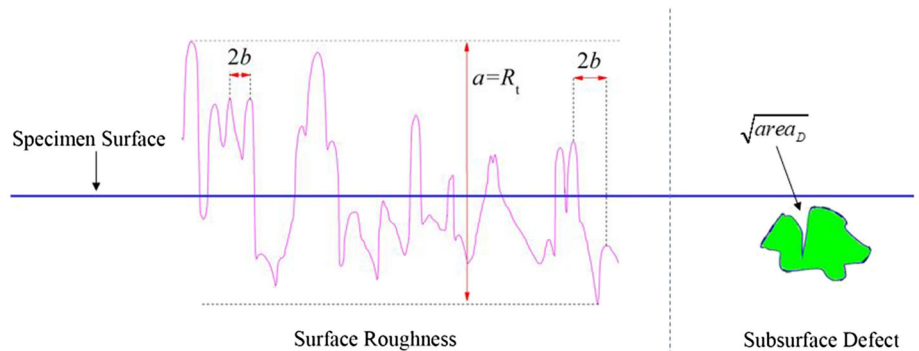

FIGURE 10 Schematic showing effective defect parameter. [Colour figure can be viewed at wileyonlinelibrary.com]

surface roughness $\sqrt{area}_R$ of as-built specimens can be calculated by using Equation (5) since the value of $\frac{a}{2b}$ is larger than 0.195.

For quantifying the effect of surface roughness on the fatigue performance of L-PBF Ti-6Al-4V, a stress concentration factor was employed and is expressed as follows[66]:

$$K_t = 1 + 2\sqrt{\frac{d}{r}} \qquad (6)$$

where r represents a root radius of elliptical surface micro-notch and d is notch depth assumed to be the maximum depth of valleys $R_t/2$. Based on the SWLI images, the notch radius r was obtained as 26.1 μm for as-built specimens, but 82.9 μm for surface-polished specimens. Similarly, the notch depth d was 31.6 μm for as-built specimens and 3.45 μm for surface-polished specimens. Therefore, the stress concentration factors can be

calculated to be 3.2 and 1.4 for as-built and surface-polished specimens, respectively. It is sure that the stress concentration at the surface roughness of as-built specimens is larger than that of surface-polished specimens, which leads to fatigue crack initiation easier for as-built specimens than that for surface-polished specimens.

The effects of equivalent size ($\sqrt{area}$) and depth (defined as the distance from defect center to specimen surface) of the defects on fatigue crack initiation of L-PBF Ti-6Al-4V under different surface roughness (as-built and surface-polished) and stress ratios ($R = -1$ and 0.7) are also investigated. Figure 11A presents the relations between fatigue life N_f and $\sqrt{area}$, in which the values of the $\sqrt{area}$ for as-built specimens are in the range of 110–148 μm and the fatigue lives are in the range of 6×10^4–3×10^6 cycles, namely, in HCF regime. For surface-polished specimens at $R = 0.7$, the values of $\sqrt{area}$ are in the range of 49–100 μm and the fatigue lives
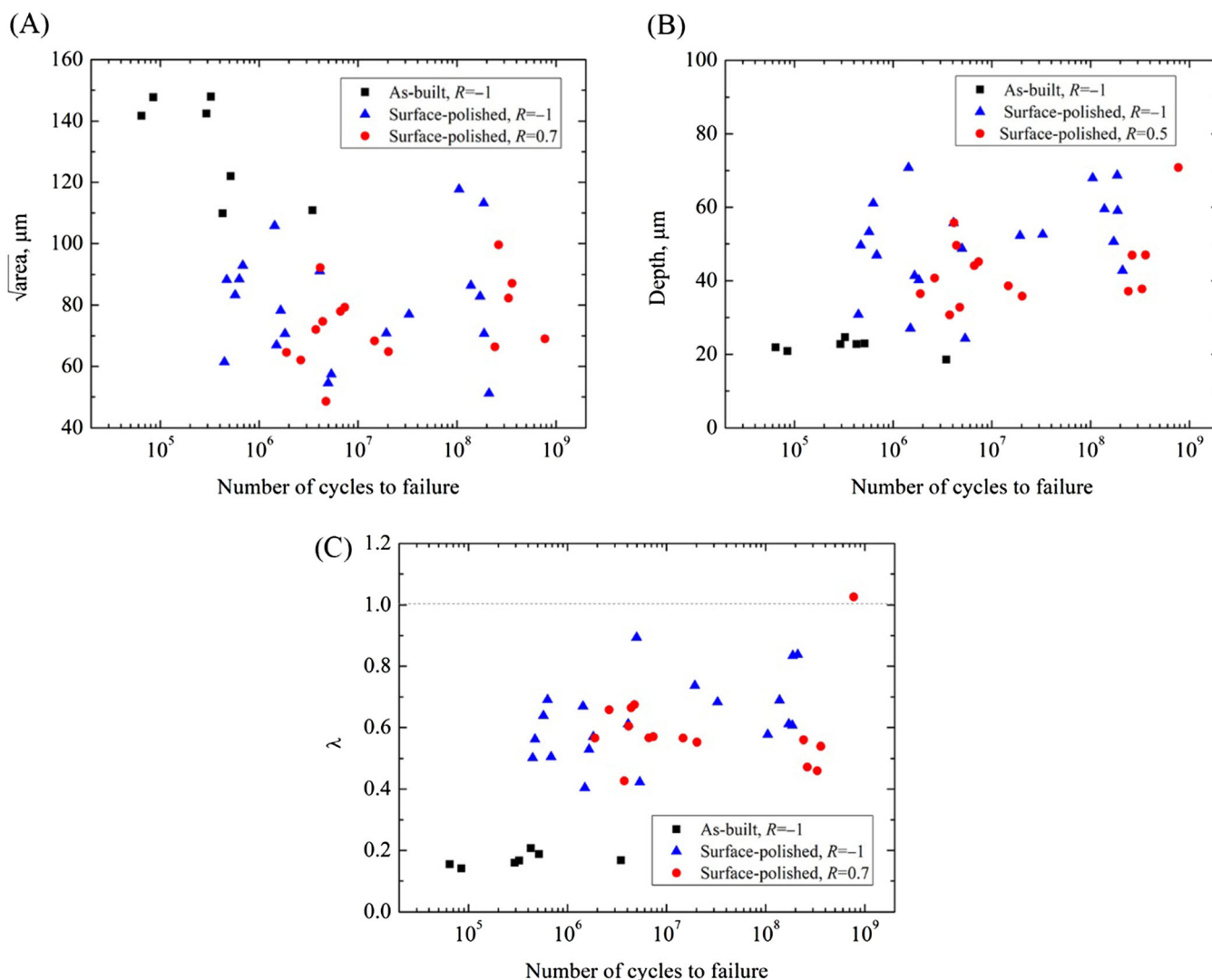

FIGURE 11 Variations of $\sqrt{area}$ (A), depth (B), and parameter λ (C) with the number of cycles to failure. [Colour figure can be viewed at wileyonlinelibrary.com]

are in a wide range of 2×10^6–8×10^9 cycles, namely, in both HCF and VHCF regimes. For surface-polished specimens at $R = -1$, the values of $\sqrt{area}$ are in the range of 51–118 µm and the fatigue lives are in a wide range of 4×10^5–2×10^8 cycles, namely, in both HCF and VHCF regimes. It is seen that the values of $\sqrt{area}$ present a large scattering for surface-polished specimens and as-built specimens. Moreover, the values of $\sqrt{area}$ for as-built specimens are distinctly larger than that of surface-polished specimens due to the interaction between surface roughness and subsurface defects in as-built specimens. It indicates that surface roughness has a significant effect on the equivalent defect size to induce fatigue crack initiation of L-PBF Ti-6Al-4V. Nevertheless, the values of $\sqrt{area}$ of surface-polished specimens show no clear distinction between the cases of $R = -1$ and 0.7, suggesting that stress ratio has an insignificant effect on the equivalent defect size to induce fatigue crack initiation of L-PBF Ti-6Al-4V. Figure 11B presents the relations between fatigue life N_f and defect depth, in which the values of the defect depth for as-built specimens vary in a narrow range of 18–25 µm in HCF regime. For surface-polished specimens in both HCF and VHCF regimes, the values of the defect depth vary in the range of 31–71 µm at $R = 0.7$, but the range of 24–71 µm at $R = -1$. It is obvious that the values of the defect depth display a big scattering for surface-polished specimens. In addition, the defect depth of as-built specimens in general is much smaller than that of surface-polished specimens, showing that surface roughness has a considerable effect on the depth of the defect that induced fatigue crack initiation of L-PBF Ti-6Al-4V. For surface-polished specimens under these two stress ratios, the values of the defect depth vary in the same range, inferring that stress ratio has little effect on the depth of the defect that

induced fatigue crack initiation. Since the values of equivalent defect size ($\sqrt{area}$) and defect depth present large scattering, a dimensionless parameter λ (depth/$\sqrt{area}$)[56] was employed to further quantify the relationship between them. It is seen from Figure 11C that the values of λ for most data points are less than 1 except one point, implying that crack initiation prefers to start from the defects at subsurface region in both HCF and VHCF regimes, which agrees with the experimental results shown in Section 3.4.

4.2 | Threshold values of stress intensity factor for surface and subsurface defects

Fatigue cracks tend to initiate and early propagate at the defects with large stress concentration in L-PBF Ti-6Al-4V. In order to quantitatively analyze the early propagation of the fatigue crack of L-PBF Ti-6Al-4V, the stress intensity factor range (ΔK) at the fatigue crack tip is used.[67] The defect to induce the fatigue crack initiation is regarded as an initial crack. Hence, ΔK of the defect is denoted as ΔK_d, which is calculated by[67]

$$\Delta K_d = \lambda \sigma_a \sqrt{\pi \sqrt{area}} \qquad (7)$$

where σ_a is the stress amplitude (MPa), λ is 0.65 for surface defects and 0.50 for subsurface defects, and $\sqrt{area}$ (m) is the square root of the projected area of the defect on a plane perpendicular to the loading direction.[67]

By using Equation (7), the values of ΔK_d are obtained and the relations among ΔK_d, N_f, and $\sqrt{area}$ are shown in Figure 12 for the cases of different surface roughness (as-built and surface-polished) and stress ratios ($R = -1$
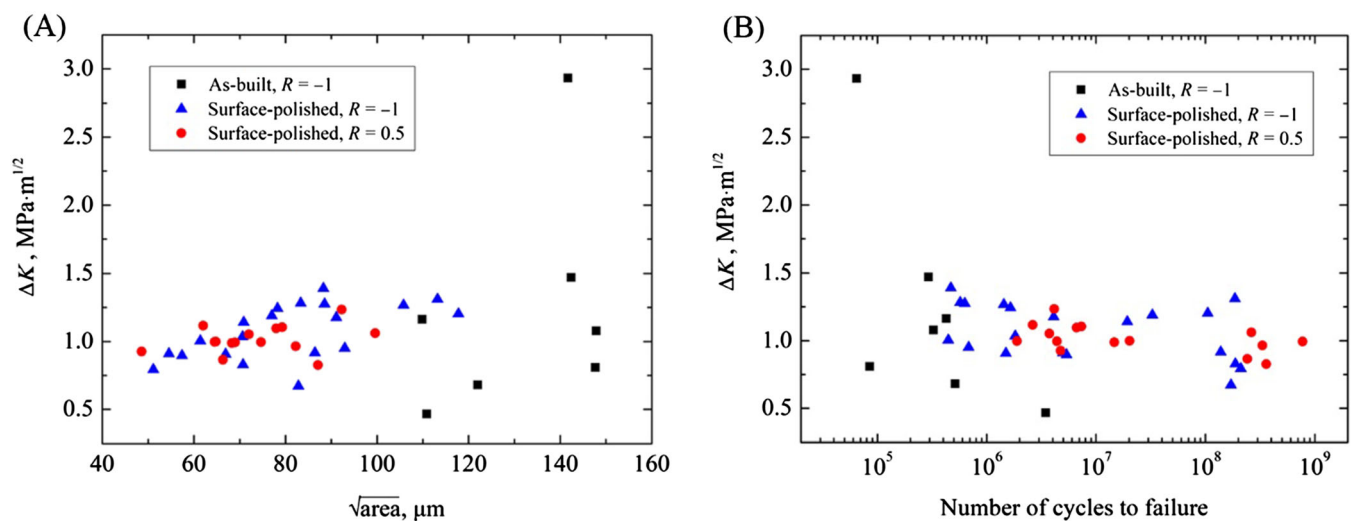

FIGURE 12 (A) ΔK_d versus $\sqrt{area}$, and (B) ΔK_d versus N_f. [Colour figure can be viewed at wileyonlinelibrary.com]

and 0.7). Figure 12A shows the relation between ΔK_d and N_f. It is seen that the values of ΔK_d for most as-built specimens are in the range of 0.5–1.5 MPa·m$^{1/2}$ with one exceptional value of 2.9 MPa·m$^{1/2}$, and the fatigue lives N_f for all as-built specimens are in the range of 6×10^4–3×10^6 cycles, that is, within HCF regime. For surface-polished specimens at $R = -1$, the values of ΔK_d are in the range of 0.7–1.4 MPa·m$^{1/2}$, and the fatigue lives N_f are in a wide range of 4×10^5–2×10^8 cycles, that is, within both HCF and VHCF regimes. For surface-polished specimens at $R = 0.7$, the values of ΔK_d are in the range of 0.8–1.2 MPa·m$^{1/2}$, and the fatigue lives N_f are in a wide range of 2×10^6–8×10^9 cycles, that is, within both HCF and VHCF regimes. It is seen that the values of ΔK_d for as-built specimens present a large scattering with the increase of fatigue life. On the contrary, the values of ΔK_d for the surface-polished specimens vary in a relatively narrow range with the increase of fatigue life, under both stress ratios of -1 and 0.7. Figure 12B illustrates the relation between ΔK_d and $\sqrt{area}$, in which the values of $\sqrt{area}$ vary in the range of 110–148 μm for as-built specimens and 49–118 μm for surface-polished specimens. The values of ΔK_d for as-built specimens present a relatively large scattering (0.5–2.9 MPa·m$^{1/2}$) even with a relatively narrow range in the values of $\sqrt{area}$. In contrast, the values of ΔK_d for surface-polished specimens present in a relatively small scattering (0.7–1.4 MPa·m$^{1/2}$) with a relatively wide range in the values of $\sqrt{area}$. Figure 12 indicates that the value of $\Delta K_{d,min}$ (the minimum value of ΔK_d) is approximately 0.7 MPa·m$^{1/2}$ for surface-polished specimens and about 0.5 MPa·m$^{1/2}$ for as-built specimens. It is suggested that the fatigue crack is easier to initiate and propagate in as-built than surface-polished L-PBF Ti-6Al-4V. In other words, surface roughness does have a considerable effect on the fatigue crack propagation of L-PBF Ti-6Al-4V. In addition, for surface-polished specimens, the value of $\Delta K_{d,min}$ is 0.7 MPa·m$^{1/2}$ for the case of $R = -1$ and 0.8 MPa·m$^{1/2}$ for the case of $R = 0.7$, indicating that stress ratio has little effect on the fatigue crack propagation of L-PBF Ti-6Al-4V.

5 | CONCLUSIONS

In this research, the fatigue behavior of L-PBF Ti-6Al-4V with defect-enriched subsurface layer in both HCF and VHCF regimes was investigated under two stress ratios ($R = -1$ and 0.7) and two states of surface roughness (as-built and surface-polished). The main conclusions are listed as follows:

1. The *S-N* data display a descending trend for L-PBF Ti-6Al-4V at different stress ratios and surface roughness. The values of fatigue strength of surface-polished specimens are evidently higher than those of as-built specimens in HCF and VHCF regimes.

2. Fatigue cracks initiate from the subsurface or defect-enriched layer of L-PBF Ti-6Al-4V due to the interaction between surface roughness and subsurface defects. Surface roughness has a significant effect on fatigue crack initiation, whereas stress ratio has little effect on the type of crack initiation for surface-polished L-PBF Ti-6Al-4V in HCF and VHCF regimes.

3. The values of equivalent sizes ($\sqrt{area}$) and the depths of defects inducing crack initiation present large scattering. The equivalent defect size of as-built L-PBF Ti-6Al-4V is considerably larger than that of surface-polished L-PBF Ti-6Al-4V, but the defect depth of as-built L-PBF Ti-6Al-4V is much smaller than that of surface-polished L-PBF Ti-6Al-4V.

4. The value of $\Delta K_{d,min}$ for surface-polished L-PBF Ti-6Al-4V is larger than that of as-built L-PBF Ti-6Al-4V, suggesting that the fatigue crack is easier to propagate in as-built L-PBF Ti-6Al-4V than in surface-polished L-PBF Ti-6Al-4V. For surface-polished L-PBF Ti-6Al-4V, the values of $\Delta K_{d,min}$ at $R = -1$ and 0.7 are very close, suggesting that the fatigue crack has almost the same resistance to crack propagation under these two stress ratios.

In general, this paper pays specific attention to the effect of the defects, which are in the subsurface layer induced by the contour scanning in L-PBF process, on HCF and VHCF fatigue performance. This is useful information for the case that the subsurface defects of AMed parts are hardly or impossible to be eliminated.

CONFLICT OF INTEREST STATEMENT
The authors declare that they have no known competing financial interests or personal relationships that could have appeared to influence the work reported in this paper.

DATA AVAILABILITY STATEMENT
The data in this paper are available from the corresponding author and the first author upon reasonable request.

NOMENCLATURE

AM	additive manufacturing
CSAM	cold spray additive manufacturing
d	layer thickness
DED	directed energy deposition
E	energy density
EB-PBF	electron beam powder bed fusion
EBSD	electron backscattered diffraction
h	hatch spacing
HCF	high-cycle fatigue
HIP	hot-isostatic-pressing
HV	Vickers hardness
LOF	lack-of-fusion
L-PBF	laser powder bed fusion
N_f	number of cycles to failure
P	laser power
R	stress ratio
R_a	average roughness
R_t	maximum height of surface profile
RA	rough area
SEM	scanning electron microscopy
SWLI	scanning white light interferometer
V	scan speed
VHCF	very-high-cycle fatigue
σ_a	stress amplitude
σ_b	tensile strength
σ_{max}	maximum stress
σ_y	yield strength
ΔK	stress intensity factor range
$\sqrt{area}$	equivalent size of subsurface defect inducing the fatigue crack initiation

ORCID

Youshi Hong https://orcid.org/0000-0003-3425-6808

REFERENCES

1. Frazier WE. Metal additive manufacturing: a review. *J Mater Eng Perf*. 2014;23(6):1917-1928.
2. Murr LE, Quinones SA, Gaytan SM, et al. Microstructure and mechanical behavior of Ti-6Al-4V produced by rapid-layer manufacturing for biomedical applications. *J Mech Behav Biomed Mater*. 2009;2(1):20-32.
3. ASTM. Standard F2792-12a: Standard terminology for additive manufacturing technologies, 2012.
4. Lewandowski JJ, Seifi M. Metal additive manufacturing: a review of mechanical properties. *Annu Rev Mat Res*. 2016; 46(1):151-186.
5. Shipley H, McDonnell D, Culleton M, et al. Optimisation of process parameters to address fundamental challenges during selective laser melting of Ti-6Al-4V: a review. *Int J Mach Tool Manuf*. 2018;128:1-20.
6. Liu SY, Shin YC. Additive manufacturing of Ti-6Al-4V alloy: a review. *Mater des*. 2019;164:107552.
7. Sanaei N, Fatemi A. Defect-based multiaxial fatigue life prediction of L-PBF additive manufactured metals. *Fatigue Fract Eng Mater Struct*. 2021;44(7):1897-1915.
8. Xu W, Brandt M, Sun S, et al. Additive manufacturing of strong and ductile Ti–6Al–4V by selective laser melting via in situ martensite decomposition. *Acta Mater*. 2015;85:74-84.
9. Ladani L, Sadeghilaridjani M. Review of powder bed fusion additive manufacturing for metals. *Metals*. 2021;11(9):1391.
10. Chern AH, Nandwana P, Yuan T, et al. A review on the fatigue behavior of Ti-6Al-4V fabricated by electron beam melting additive manufacturing. *Int J Fatigue*. 2019;119:173-184.
11. Franchitti S, Pirozzi C, Borrelli R. Influence of hot isostatic pressing and surface finish on the mechanical behaviour of Ti6Al4V processed by electron beam melting. *Fatigue Fract Eng Mater Struct*. 2020;43(12):2828-2841.
12. Segersäll M, Kerwin A, Hardaker A, Kahlin M, Moverare J. Fatigue response dependence of thickness measurement methods for additively manufactured E-PBF Ti-6Al-4V. *Fatigue Fract Eng Mater Struct*. 2021;44(7):1931-1943.
13. Hattingh DG, Botha S, Bernard D, James MN, du Plessis A. Corrosion fatigue of Ti-6Al-4V coupons manufactured by directed energy deposition. *Fatigue Fract Eng Mater Struct*. 2022;45(7):1969-1980.
14. Carroll BE, Palmera TA, Beese AM. Anisotropic tensile behavior of Ti-6Al-4V components fabricated with directed energy deposition additive manufacturing. *Acta Mater*. 2015;87: 309-320.
15. Ren Y, Lin X, Guo P, et al. Low cycle fatigue properties of Ti-6Al-4V alloy fabricated by high-power laser directed energy deposition: experimental and prediction. *Int J Fatigue*. 2019; 127:58-73.
16. Yuan L, Ding S, Wen C. Additive manufacturing technology for porous metal implant applications and triple minimal surface structures: a review. *Bioactive Mater*. 2019;4(1):56-70.
17. Li G, Chandra S, Rashid R, Palanisamy S, Ding S. Machinability of additively manufactured titanium alloys: a comprehensive review. *J Manuf Process*. 2022;75:72-99.
18. Kuwaki K, Tsukamoto M, Komatsu K, Sakata J, Abe T. Ten year clinical experience with the carbomedics heart valve implants. *Artif Organs*. 2002;26(8):695-702.
19. Witek L. Failure analysis of turbine disc of an aero engine. *Eng Fail Anal*. 2006;13(1):9-17.
20. Sanaei N, Fatemi A. Analysis of the effect of surface roughness on fatigue performance of powder bed fusion additive manufactured metals. *Theor Appl Fract Mech*. 2020; 108:102638.
21. Du L, Qian G, Zheng L, Hong Y. Influence of processing parameters of selective laser melting on high-cycle and very-high-cycle fatigue behaviour of Ti-6Al-4V. *Fatigue Fract Eng Mater Struct*. 2021;44(1):240-256.
22. Li P, Warner DH, Fatemi A, Phan N. Critical assessment of the fatigue performance of additively manufactured Ti-6Al-4V and perspective for future research. *Int J Fatigue*. 2016;85: 130-143.
23. Sanaei N, Fatemi A. Analysis of the effect of internal defects on fatigue performance of additive manufactured metals. *Mater Sci Eng A*. 2020;785:139385.
24. Greitemeier D, Donne CD, Syassen F, Eufinger J, Melz T. Effect of surface roughness on fatigue performance of additive

manufactured Ti-6Al-4V. *Mater Sci Technol*. 2016;32(7): 629-634.

25. Günther J, Leuders S, Koppa P, et al. On the effect of internal channels and surface roughness on the high-cycle fatigue performance of Ti-6Al-4V processed by SLM. *Mater Des*. 2018; 143:1-11.

26. Vayssette B, Saintier N, Brugger C, El May M. Surface roughness effect of SLM and EBM Ti-6Al-4V on multiaxial high cycle fatigue. *Theor Appl Fract Mech*. 2020;108:102581.

27. Kelly C, Evans N, Irvin C, Chapman S, Gall K, Safranski D. The effect of surface topography and porosity on the tensile fatigue of 3D printed Ti-6Al-4V fabricated by selective laser melting. *Mater Sci Eng C*. 2019;98:726-736.

28. Pegues J, Roach M, Scott Williamson R, Shamsaei N. Surface roughness effects on the fatigue strength of additively manufactured Ti-6Al-4V. *Int J Fatigue*. 2018;116:543-552.

29. Townsend A, Senin N, Blunt L, Leach RK, Taylor JS. Surface texture metrology for metal additive manufacturing: a review. *Precis Eng*. 2016;46:34-47.

30. Zhang J, Fatemi A. Surface roughness effect on multiaxial fatigue behavior of additive manufactured metals and its modeling. *Theor Appl Fract Mech*. 2019;103:102260.

31. Lee S, Pegues JW, Shamsaei N. Fatigue behavior and modeling for additive manufactured 304L stainless steel: the effect of surface roughness. *Int J Fatigue*. 2020;141:105856.

32. Lee S, Rasoolian B, Silva DF, Pegues JW, Shamsaei N. Surface roughness parameter and modeling for fatigue behavior of additive manufactured parts: a non-destructive data-driven approach. *Addit Manuf*. 2021;46:102094.

33. Schneller W, Leitner M, Pomberger S, et al. Fatigue strength assessment of additively manufactured metallic structures considering bulk and surface layer characteristics. *Addit Manuf*. 2021;40:101930.

34. Yadollahi A, Mahtabi MJ, Khalili A, Doude HR Jr, Newman JC. Fatigue life prediction of additively manufactured material: effects of surface roughness, defect size, and shape. *Fatigue Fract Eng Mater Struct*. 2018;41(7):1602-1614.

35. Masuo H, Tanaka Y, Morokoshi S, et al. Influence of defects, surface roughness and HIP on the fatigue strength of Ti-6Al-4V manufactured by additive manufacturing. *Int J Fatigue*. 2018; 117:163-179.

36. Borrego LP, Jesus J, Ferreira JAM, Costa JDM, Capela C. Assessment of the fatigue performance of heat-treated addictive manufactured Ti-6Al-4V specimens. *Procedia Struct Integr*. 2019;18:651-656.

37. Yu H, Li F, Wang Z, Zeng X. Fatigue performances of selective laser melted Ti-6Al-4V alloy: influence of surface finishing, hot isostatic pressing and heat treatments. *Int J Fatigue*. 2019;120: 175-183.

38. Molaei R, Fatemi A, Phan N. Significance of hot isostatic pressing (HIP) on multiaxial deformation and fatigue behaviors of additive manufactured Ti-6Al-4V including build orientation and surface roughness effects. *Int J Fatigue*. 2018; 117:352-370.

39. Macallister N, Becker TH. Fatigue life estimation of additively manufactured Ti-6Al-4V: sensitivity, scatter and defect description in damage-tolerant models. *Acta Mater*. 2022;237: 118189.

40. Sanaei N, Fatemi A. Defect-based fatigue life prediction of L-PBF additive manufactured metals. *Eng Fract Mech*. 2021; 244:107541.

41. Hong Y, Sun C. The nature and the mechanism of crack initiation and early growth for very-high-cycle fatigue of metallic materials - an overview. *Theor Appl Fract Mech*. 2017;92: 331-350.

42. Shiozawa K, Lu L. Very high-cycle fatigue behaviour of shot-peened high-carbon-chromium bearing steel. *Fatigue Fract Eng Mater Struct*. 2002;25(8-9):813-822.

43. Yang K, Huang Q, Wang Q, Chen Q. Competing crack initiation behaviors of a laser additively manufactured nickel-based superalloy in high and very high cycle fatigue regimes. *Int J Fatigue*. 2020;136:105580.

44. Hong Y, Liu X, Lei Z, Sun C. The formation mechanism of characteristic region at crack initiation for very-high-cycle fatigue of high-strength steels. *Int J Fatigue*. 2016;89:108-118.

45. Sakai T, Oguma N, Morikawa A. Microscopic and nanoscopic observations of metallurgical structures around inclusions at interior crack initiation site for a bearing steel in very high-cycle fatigue. *Fatigue Fract Eng Mater Struct*. 2015;38(11): 1305-1314.

46. Schönbauer BM, Ghosh S, Kömi J, Frondelius T, Mayer H. Influence of small defects and nonmetallic inclusions on the high and very high cycle fatigue strength of an ultrahigh-strength steel. *Fatigue Fract Eng Mater Struct*. 2021;44(11): 2990-3007.

47. Liu X, Sun C, Hong Y. Effects of stress ratio on high-cycle and very-high-cycle fatigue behavior of a Ti-6Al-4V alloy. *Mater Sci Eng A*. 2015;622:228-235.

48. Szczepanski CJ, Jha SK, Larsen JM, Jones JW. Microstructural influences on very-high-cycle fatigue crack initiation in Ti-6246. *Metall Mater Trans A*. 2008;39(12):2841-2851.

49. Molaei R, Fatemia A, Phan N, et al. Fatigue of additive manufactured Ti-6Al-4V, part II: the relationship between microstructure, material cyclic properties, and component performance. *Int J Fatigue*. 2020;132:105363.

50. Jesus J, Borrego L, Ferreira J, Costa J, Capela C. Fatigue crack growth behaviour in Ti6Al4V alloy specimens produced by selective laser melting. *Int J Fract*. 2020;223(1-2):123-133.

51. Zhai Y, Lados D, Brown E, Vigilante G. Fatigue crack growth behavior and microstructural mechanisms in Ti-6Al-4V manufactured by laser engineered net shaping. *Int J Fatigue*. 2016;93: 51-63.

52. Wu L, Jiao Z, Yu H. Study on fatigue crack growth behavior of selective laser-melted Ti6Al4V under different build directions, stress ratios, and temperatures. *Fatigue Fract Eng Mater Struct*. 2022;45(5):1421-1434.

53. Benedetti M, Fontanari V, Bandini M, Zanini F, Carmignato S. Low-and high-cycle fatigue resistance of Ti-6Al-4V ELI additively manufactured via selective laser melting: mean stress and defect sensitivity. *Int J Fatigue*. 2018;107:96-109.

54. Du L, Pan X, Qian G, Zheng L, Hong Y. Crack initiation mechanisms under two stress ratios up to very-high-cycle fatigue regime for a selective laser melted Ti-6Al-4V. *Int J Fatigue*. 2021;149:106294.

55. Krijger J, Rans C, Hooreweder B, Lietaert K, Pouran B, Zadpoor A. Effects of applied stress ratio on the fatigue

behavior of additively manufactured porous biomaterials under compressive loading. *J Mech Behav Biomed Mater*. 2017;70: 7-16.

56. Fu R, Zheng L, Ling C, Zhong Z, Hong Y. An experimental investigation of fatigue performance and crack initiation characteristics for an SLMed Ti-6Al-4V under different stress ratios up to very-high-cycle regime. *Int J Fatigue*. 2022;164: 107119.

57. Thijs L, Verhaeghe F, Craeghs T, Van Humbeeck J, Kruth J. A study of the microstructural evolution during selective laser melting of Ti-6Al-4V. *Acta Mater*. 2010;58(9):3303-3312.

58. Thompson SM, Bian L, Shamsaei N, Yadollahi A. An overview of direct laser deposition for additive manufacturing; part I: transport phenomena, modeling, and diagnostics. *Addit Manuf*. 2015;8:36-62.

59. Liu X, Sun C, Zhou Y, Hong Y. Effects of microstructure and stress ratio on high-cycle and very-high-cycle fatigue behavior of Ti-6Al-4V alloy. *Acta Metall Sin*. 2016;52:923-930.

60. Gong H, Rafi K, Gu H, Starr T, Stucker B. Analysis of defect generation in Ti-6Al-4V parts made using powder bed fusion additive manufacturing processes. *Addit Manuf*. 2014;1-4:87-98.

61. Murakami Y. *Metal fatigue: effects of small defects and nonmetallic inclusions*. 1st ed. Amsterdam: Elsevier; 2002.

62. Gadelmawla ES, Koura MM, Maksoud TMA, Elewa IM, Soliman HH. Roughness parameters. *J Mater Process Technol*. 2002;123(1):133-145.

63. Günther J, Krewerth D, Lippmann T, et al. Fatigue life of additively manufactured Ti-6Al-4V in the very high cycle fatigue regime. *Int J Fatigue*. 2017;94:236-245.

64. Xu Z, Liu A, Wang X. Fatigue performance differences between rolled and selective laser melted Ti6Al4V alloys. *Mater Charact*. 2022;189:111963.

65. Murakami Y, Takahashi K, Yamashita A. Quantitative evaluation of the effect of surface roughness on fatigue strength (effect of depth and pitch of roughness). *Trans Jpn Soc Mech Eng*. 1997;63(612):1612-1619.

66. Peterson RE, Plunkett R. Stress concentration factors. *J Appl Mech*. 1975;42(1):248.

67. Murakami Y, Kodama S, Konuma S. Quantitative evaluation of effects of non-metallic inclusions on fatigue strength of high strength steels. *Int J Fatigue*. 1989;11(5):291-298.